Inorganic Chemistry

Article

pubs.acs.org/IC

Structural Acid–Base Chemistry in the Metallic State: How μ_3-Neutralization Drives Interfaces and Helices in $Ti_{21}Mn_{25}$

Timothy E. Stacey and Daniel C. Fredrickson*

Department of Chemistry, University of Wisconsin—Madison, 1101 University Avenue, Madison, Wisconsin 53706, United States

Supporting Information

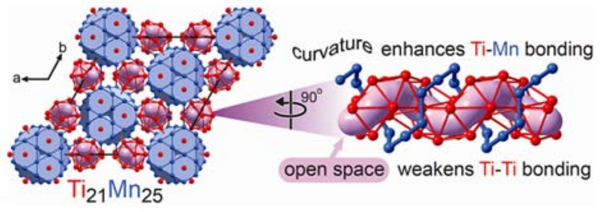

ABSTRACT: Intermetallic phases remain a large class of compounds whose vast structural diversity is unaccounted for by chemical theory. A recent resurgence of interest in intermetallics, due to their potential in such applications as catalysis and thermoelectricity, has intensified the need for models connecting their compositions to their structures and stability. In this Article, we illustrate how the μ_3-acidity model, an extension of the acid/base concept based on the Method of Moments, offers intuitive explanations for puzzling structural progressions occurring in intermetallics formed between transition metals. Simple CsCl-type structures are frequently observed for phases with near 1:1 ratios of transition metals. However, in two compounds, TiCu and $Ti_{21}Mn_{25}$, structures are adopted which deviate from this norm. μ_3-Acidity analysis shows that the formation of CsCl-type phases in these exceptional systems would yield an imbalance in the acid/base strength pairing, resulting in overneutralization of the weaker partner and thus instability. Intriguing geometrical features emerge in response, which serve to improve the neutralization of the constituent elements. In both TiCu and $Ti_{21}Mn_{25}$, part of the structure shields weaker acids or bases from their stronger partners by enhancing homoatomic bonding in the sublattice of the weaker acid or base. In TiCu, this protection is accomplished by developing doubled layers of Ti atoms to reduce their heteroatomic contacts. In $Ti_{21}Mn_{25}$ the structural response is more extreme: Ti-poor $TiMn_2$ domains are formed to guard Mn from the Ti atoms, while the remaining Ti segregates to regions between the $TiMn_2$ domains. The geometrical details of this arrangement fine-tune the acid/base interactions for an even greater level of stability. The most striking of these occurs in the Ti-rich region, where a paucity of Mn neighbors leads to difficulty in achieving strong neutralization. The Ti atoms arrange themselves in helical tubes, maximizing the surface area for Ti−Mn interactions. Through these examples, we show how the μ_3-acidity model provides simple explanations for some of the beautiful structural motifs observed in intermetallic crystals. The foundation of the model in the Method of Moments makes it applicable to a variety of other contexts, including glasses, defects, and nanostructured surfaces.

■ INTRODUCTION

Intermetallics display an immense structural diversity, which chemical theory still struggles to rationalize, let alone guide experimentalists to new structures and properties. A new urgency for understanding how structure, bonding, and reactivity are connected in these compounds has been sparked by a renewed interest in the metallic state for a variety of applications. The nanostructuring of alloys and intermetallics has led to promising new approaches to the design of devices for energy generation, use, and storage,[1−11] as well as exciting developments in catalytic activity and selectivity.[12−21] Intermetallics by themselves have also been increasingly recognized as a route to ordering metal atoms on surfaces for specialized catalytic properties, or to provide alternatives to rare and expensive metals.[22−25]

Alongside theoretical tools for analyzing bonding in solid state structures, such as the crystal orbital overlap and Hamilton populations (COOP[26,27] and COHP[28]), and the electron localization function and indicator (ELF[29−31] and ELI[32−35]), analogies to molecular chemistry have been invaluable in bridging the gap between our conceptual understanding of intermetallic structures and the rapidly expanding structural chemistry revealed by synthetic efforts. The most productive of these is the Zintl concept,[36−38] an evocation of ionization and covalent bonds to explain the structures arising from polar combinations of metals. However, the Zintl concept and other models proffered for intermetallics hardly exhaust the great richness of bonding concepts offered by chemical theory. The ground is fertile for the growth of new connections to molecular bonding.

The notion of acidity, another molecular concept, has received much less attention with regard to intermetallic phases. Several applications of acidity to the solid state and metals have been made. These include extending the Lewis theory to view late and early transition metals as, respectively, electron pair donors and acceptors,[39] and the development of a DFT-based approach to calculate site acidities and basicities.[40] Despite these advances, the full potential of acidity concept to make sense of the intermetallic realm has yet to be explored.

Received: November 29, 2012
Published: January 31, 2013

Recently, we described the mathematical basis for framing the acids and bases concept in a form that offers new ways of understanding the stability of intermetallics.[41] This approach is based on the Method of Moments as applied to DFT-calibrated Hückel calculations, and recognizes that the third moment (μ_3) of a transition metal's (TM's) density of states (DOS) distribution predicts an ideal electron count. The deviations of the actual electron count from this ideal resemble the electron-poor and -rich character of molecular Lewis acids and bases,[42] respectively. Metals that are electron poor compared to the ideal can be characterized as μ_3-acids, with the electron-rich metals then being μ_3-bases. Across the 3d series, a whole spectrum of acidity is encountered, from μ_3-acidic (Sc, Ti, V), to neutral (Cr), to basic (Mn, Fe, Co, Ni, Cu). In this scheme, intermetallic phase formation plays the role of neutralization reaction: incorporation into binary compounds reduces the μ_3-acidity/basicity of the participating elements.

As intermetallic phases are a structurally diverse class of compounds, a question that naturally arises is to what extent μ_3-neutralization determines not only the stability of a phase but also its structural features. This is the question we will address in this Article. We begin by returning to one of our earlier illustrations of the μ_3-acidity approach: determining the stability range of the simple, common CsCl type phases formed between μ_3-acidic TMs (Sc, Ti, V, Cr) and μ_3-basic TMs (Cu, Ni, Co, Fe, Mn, Cr).

The predicted stability range is shown again in Figure 1,[41,43,44] where the unresolved acidity calculated for acid/base pairs in the CsCl-type is plotted, as a function of the strengths of the component acid and base. Residual acidity is most minimized at the upper left region of the graph (dark gray). This minimum extends diagonally to the lower right-hand side, creating a valley that roughly divides the graph in half. Moving down the minimum valley away from ScCu, the participating elements decrease in acidity and basicity together, emphasizing that neutralization stems from an appropriate strength pairing.

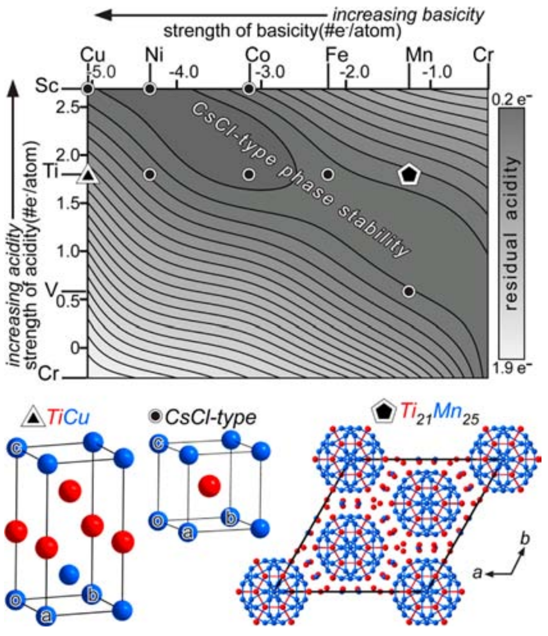

Figure 1. Structure map illustrating the correlation between low residual μ_3-acidity calculated for CsCl-type TM binaries and the experimental observation of such phases (circular points; high temperature phases are not included to minimize the role of entropy). Modified from ref 41, with permission of the American Chemical Society.[43] Also plotted in the map are points corresponding to the phases TiCu and $Ti_{21}Mn_{25}$, whose structures are pictured below the map (red spheres, μ_3-acidic elements; blue spheres, μ_3-basic elements). See note 44 for additional non-CsCl-type 1:1 phases.

The experimentally observed CsCl-type phases (leaving out high-temperature phases to avoid entropy-stabilized compounds) correlate qualitatively well with the region of minimized residual acidity on the contour map. Good neutralization is thus confirmed as an indicator of phase formation, while poor neutralization is an indicator of no CsCl-type phase forming for these systems.

What about other structures? In this Article, we will return to the CsCl map in Figure 1, this time focusing on what happens structurally as we move out of the valley of low residual acidity. Along the rims of this valley, two other phases at or close to a 1:1 stoichiometry are found to form in the Ti−Cu and Ti−Mn systems, but with significantly different structure types. TiCu adopts a bcc-like arrangement as in the CsCl type,[45] but the atoms are reordered to double the length of the unit cell in the *c* direction. A survey of the Ti−Mn binary phases reveals that two phases form with near 1:1 stoichiometries, located at 50.5% and 52% atomic percent Mn, respectively.[46] Neither adopt the CsCl structure, and only the phase with higher Mn content has been completely solved: the $Zr_{21}Re_{25}$-type $Ti_{21}Mn_{25}$ possesses a relatively large rhombohedral unit cell with dimensions of a = 23.596 Å and c = 8.035 Å, containing infinite columns of the $MgZn_2$ structure.[47]

In what way are these new structures related to their placement at the edges of the CsCl-type stability domain? As we will see below, the concept of μ_3-acids and bases offers a visual and intuitive explanation for the unusual geometries preferred by TiCu and $Ti_{21}Mn_{25}$. In this model, the crystal structure becomes a malleable property, through which the balance of heteroatomic and homoatomic interactions can be tuned for optimal neutralization. Interfaces, antiphase boundaries, and helices will appear as different structural means for achieving this balance. Our first step in developing this picture is to take a closer look at how μ_3-neutralization and structure are related through the Method of Moments.

■ COMPUTATIONAL METHODS

The band energies and electronic density of states (DOS) curves from DFT calculations form the starting point for a μ_3-acidity analysis. These were calculated for each of the compounds discussed in this Article with the Vienna Ab Initio Simulation Package (VASP),[48−51] using the generalized gradient approximation (GGA) of Perdew and Wang (PW91),[52,53] and the projector augmented wave (PAW) potentials provided with the program.[54,55] Prior to the calculation of the ground state properties, full optimizations of the unit cell parameters and atomic coordinates were carried out.

The GGA-DFT band energies and DOS curves then served as a basis for the parametrization of Hückel models using our program *eHtuner*.[56] The Hückel calculations themselves were performed with the YAeHMOP program.[57] Hamiltonian matrix elements obtained from the best-fit Hückel models provide the input for tracing the values of the moments of the DOS (μ_n) to particular geometrical features.

Details of the GGA-DFT calculations (including the k-point meshes and energy cut-offs used) and tables of the Hückel parameters obtained are provided in the Supporting Information.

■ μ_3-ACIDITY AND STABILITY

The Method of Moments applied to Hückel/orthogonal tight-binding calculations provides a connection between a structure's local topology of orbital interactions and the shape of its electronic density of states (DOS) distribution.[58−61] Here, structure and electronics are bridged by the moments of the DOS curve, μ_n:

$$\mu_n = \int_{\infty}^{-\infty} E^n \mathrm{DOS}(E)\, \mathrm{d}E \qquad (1)$$

The lowest order moments measure simple statistical quantities, such as the area of the distribution (μ_0), its mean value (μ_1), and its variance (μ_2). As we move to higher moments, other aspects of the curve's shape are described such that the infinite set of moments, $\{\mu_0, \mu_1, \mu_2, ..., \mu_\infty\}$, uniquely defines the entire distribution. To focus on the effect of higher moments, it is customary to standardize μ_0, μ_1, and μ_2 to 1, 0, and 1, respectively.[62] Standardizing moments μ_0 through μ_2 in this way adjusts the axes of the DOS curve so that the energies are measured in units of the standard deviations (σ) from the mean value of the DOS.

The third moment, μ_3, is closely tied to the optimal electron count of a system. This is illustrated in Figure 2 by comparing DOS curves with $\mu_3 = 0$, $\mu_3 > 0$, and $\mu_3 < 0$. For all three, a pseudogap appears between a pair of peaks. Across this series, changing the μ_3 value shifts the number of states above and below the pseudogap. $\mu_3 = 0$ produces a totally symmetric DOS curve, $\mu_3 = -1$ moves more of the distribution above the pseudogap, and $\mu_3 = 1$ has the opposite effect, moving more of the distribution below the pseudogap. Since the μ_3 determines the number of states below the pseudogap, the μ_3 also controls the percent band filling (BF) that would populate the curve up to the pseudogap. The symmetric DOS distribution would be ideal for a 50% BF, the DOS curve with $\mu_3 = -1$ is better adapted for a lower BF, and the DOS curve with $\mu_3 = 1$ is more suitable for a BF higher than 50%.

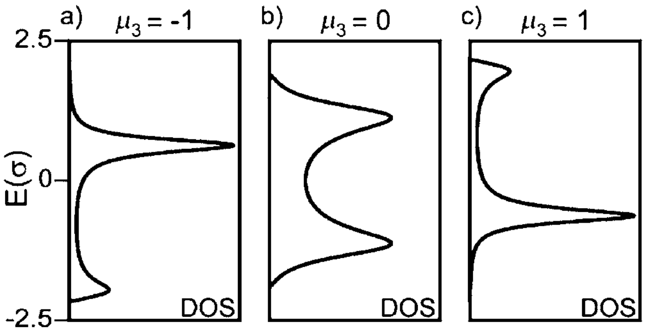

Figure 2. Influence of the third moment (μ_3) on the shape of a DOS distribution. DOS curves are constructed with μ_3 (a) less than, (b) equal to, and (c) greater than zero, with equal values for the earlier moments.

In a recent paper, we showed that this connection between BF and μ_3 can be quantified.[41] For a DOS curve defined by moments μ_0–μ_4, the optimal μ_3 value for any BF is such that the pseudogap separates the filled and empty levels. This is satisfied when

$$\mu_3 = \frac{2\mathrm{BF} - 1}{(\mathrm{BF} - \mathrm{BF}^2)^{1/2}} \qquad (2)$$

This can be reversed to say that for any μ_3 value, the optimal BF is

$$\mathrm{BF}_{\mathrm{ideal}} = \frac{1}{2} + \frac{\mu_3}{2\sqrt{\mu_3^2 + 4}} \qquad (3)$$

Thus, the μ_3 of a DOS distribution dictates its best occupancy, and we can measure how close or far away the calculated occupancy is from that ideal. Atoms whose electron counts correspond to BFs below this ideal would be expected to be electron deficient, in a manner analogous to Lewis acids. Likewise, atoms with electron counts greater than the ideal would be analogous to Lewis bases. The strength of this acidity/basicity is given by the atom's μ_3-acidity: the difference between its ideal and actual electron counts.

How does one set about applying these ideas? Starting with a DFT-calibrated Hückel calculation, the μ_3 value for a given atom can be calculated from its projected DOS curve, or directly from the Hückel Hamiltonian matrix (as described in the next section). μ_3 is then used to calculate $\mathrm{BF}_{\mathrm{ideal}}$ using eq 2. Finally, the μ_3-acidity is determined by taking the difference between the ideal and actual electron count.

An important consideration is the choice of basis functions to include in the analysis. As low order moment models can only reproduce simple features of the DOS distribution, the number of undulations in the distribution must be kept at a minimum. This is accomplished by limiting the basis set to only the valence orbitals most involved in reactivity and bonding. For TMs, there is a well-established precedent for focusing on the d orbitals, an approach that has been affirmed in successful descriptions of the structural chemistry and reactivity of TM-based materials.[63−65] In our μ_3-acidity analyses, we will thus use a d-orbital-only basis set. The populations of the d-orbitals are determined from DFT-calibrated Hückel calculations using a full spd valence orbital basis set.

■ MAKING μ_3 MEANINGFUL, STRUCTURALLY

Having summarized the μ_3-acidity approach in the previous section, we now turn to developing a more explicit relationship between crystal structure and μ_3-neutralization. A central advantage of using the Method of Moments as a basis for studying acidity, or any chemical property in a structure, is that the μ_n values are transparently related to the structural features of a compound. With the simplicity of Hückel theory, the μ_n's can be expressed in terms of sums of products of Hamiltonian matrix elements (H_{ij}):

$$\mu_n = \sum_{i_1} \sum_{i_2} ... \sum_{i_n} H_{i_1 i_2} H_{i_2 i_3} ... H_{i_n i_1} \qquad (4)$$

By calculating the moment this way, it can be envisioned as a sum of walks through the atomic orbitals of the structure. Each H_{ij} term represents a step between atomic orbitals along the walk. For a given moment of order n, each product within the summation is a closed path made up of n steps.[59]

For a given atom, we can calculate μ_3 of the atom's projected DOS curve using the above equation, with each walk beginning on an orbital of that atom:

$$\mu_3^{\mathrm{atom}} = \sum_{i_1 \in \mathrm{atom}} \sum_{i_2} \sum_{i_3} H_{i_1 i_2} H_{i_2 i_3} H_{i_3 i_1} \qquad (5)$$

The terms, graphically represented in Figure 3, include three atom, triangular walks involving exclusively $i \neq j$ H_{ij} components.

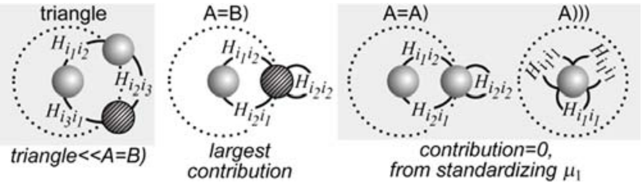

Figure 3. Schematic representation of the closed walks defined by the $H_{ij}H_{jk}H_{ki}$ terms contributing to μ_3. Triangle walks can involve any homoatomic or heteroatomic contacts. These are small since H_{ij} components are much smaller than H_{ii} components. The homoatomic walks, A=A)) and A))), become zero upon standardizing μ_0−μ_2. This leaves the A=B) components as the largest contributors to the μ_3 value.

Self-interaction terms (H_{ii}) are also allowed, which leads to the walks of forms including A=B), A=A), and A))). Here, "=" symbols correspond to two H_{ij} ($i \neq j$) components (one departing, one returning), and ")" symbols refer to an H_{ii} component. In all of these paths, we must depart from and return to the central atom in three steps. With this restriction, walks contributing to μ_3 explore only the first coordination environment. The summation of eq 5 thus corresponds to an enumeration of 3-step paths between atomic orbitals in the atom's first coordination sphere.

A large fraction of these terms vanish upon standardizing the DOS curve such that $\mu_1 = 0$. The first moment, μ_1, of an atomic DOS curve is the average energy for that distribution. When we consider a d-only basis, μ_1 is then simply the center of gravity of the atom's d-block, i.e., $\mu_1 = H_{ii}$. By setting μ_1 to zero, we then measure all other energies relative to the atom's d-orbital energy, such that the H_{ii}'s of all d-orbitals on other atoms of the same element are also zero. This affects the summation of eq 5 by eliminating all terms involving in-place steps on the central atom or any other atom of the same element.

Once these terms are eliminated, the standardized moment summation splits simply into two parts:

$$\begin{aligned}\mu_3^{\text{atom}} &= \Big[\sum_{i_1\in\text{atom}}\sum_{i_2}\sum_{i_3} H_{i_1i_2}H_{i_2i_3}H_{i_3i_1}\ (\text{with } i_1 \neq i_2 \neq i_3)\Big] \\ &\quad + \Big[\sum_{i_1\in\text{atom}}\ \sum_{i_2\in\text{B atoms}} H_{i_1i_2}H_{i_2i_2}H_{i_2i_1}\Big] \\ &= \mu_3^{\text{triangle}} + \mu_3^{\text{A=B)}} \end{aligned} \tag{6}$$

It includes those interactions that span three atoms to form a triangle, and interactions which probe the first coordination sphere and involve an in-place step on a heteroatom.

Experience has shown us that these two components are not of equal importance. Matrix elements corresponding to in-place steps are typically 10−100 times larger in magnitude, as interatomic steps are weighted by an overlap integral within the H_{ij} component, which cannot be greater than 1. Since μ_3^{triangle} terms are products of solely H_{ij} elements ($i \neq j$), their contribution to the μ_3^{atom} summation are much smaller than the $\mu_3^{\text{A=B)}}$ terms, causing $\mu_3^{\text{atom}} \approx \mu_3^{\text{A=B)}}$.

The $\mu_3^{\text{A=B)}}$ component to μ_3^{atom} can be further decomposed. The $H_{i_2i_2}$ factors present in the $\mu_3^{\text{A=B)}}$ summation equal the difference between the ionization energy of central atom A and any neighboring heteroatom, i.e. $H_{i_2i_2} = \Delta H_{ii}$. In a binary phase, this term will be the same for any heteroatomic contact around the central atom. We can then factor out ΔH_{ii} from the summation as follows:

$$\begin{aligned}\mu_3^{\text{atom,A=B)}} &= \left(\sum_{i_1\in\text{atom}}\ \sum_{i_2\in\text{B atoms}} H_{i_1i_2}H_{i_2i_1}\right)\Delta H_{ii} \\ &= \mu_2^{\text{A}-\text{B}}\Delta H_{ii}\end{aligned} \tag{7}$$

Here $\mu_2^{\text{A-B}}$ is the heteroatomic contribution to μ_2. We are left with the μ_3 of an atom expressed as a product of two factors related to heteroatomic contacts of the structure: the difference in the ionization energy between the two elements (ΔH_{ii}), and the component of the energy dispersion ($\mu_2 = \sigma^2$) generated by heteroatomic interactions ($\mu_2^{\text{A-B}}$).

To make this analysis more chemically intuitive, we can return to a conventional energy unit more familiar to chemists, the electronvolt (eV). By reincorporating the standard deviation (σ) of the atomic DOS distribution, the above equation is rewritten as

$$\begin{aligned}\mu_3^{\text{atom,A=B)}} &= \left(\mu_2^{\text{A}-\text{B}}\frac{\sigma^2}{\sigma^2}\right)\left(\Delta H_{ii}\frac{\sigma}{\sigma}\right) \\ &= \frac{\mu_2^{\text{A}-\text{B(eV)}}}{\mu_2^{\text{(eV)}}}\frac{\Delta H_{ii}^{\text{(eV)}}}{\sigma^{\text{(eV)}}}\end{aligned} \tag{8}$$

The first factor, $\mu_2^{\text{A-B}}/\mu_2$, is the relative strength of heteroatomic interactions to the strength of interactions with all neighbors within the first coordination sphere. Increasing the number of heteroatoms and decreasing their bond distance to the central atom will increase this factor. The second term, $\Delta H_{ii}/\sigma$, is the electronegativity difference between the two types of elements involved in bonding, relative to the overall spread of the distribution.

Somewhat surprisingly, this basic equation provides all we need to start exploring how structure and μ_3-neutralization are connected. As the ideal BF of a DOS curve is a function of μ_3, the above equation provides a link between an atom's optimal electron count and its coordination environment. In the next section, we will demonstrate this on the relatively simple, if unusual, structure of TiCu.

■ HOW THE TiCu STRUCTURE OPTIMIZES NEUTRALIZATION

As we saw earlier in Figure 1, the compound TiCu lies just on the outskirts of the CsCl stability domain. This is reflected in a close structural relationship between the TiCu and CsCl types, as is apparent when viewing the two structures down the *a*-direction (Figure 4a). In this view, rows of Ti atoms (red) appear as alternating with rows of Cu atoms (blue) in the CsCl type (ABABAB). In the TiCu type, a similar alternation is seen, but this time rows of Ti and Cu are doubled (AABBAABB). This ordering can be interpreted as arising from the presence of antiphase boundaries in the CsCl-type structure at every other layer. In the coming paragraphs, we will show that these antiphase boundaries can be simply explained using the structure-bonding relationships derived in the last section.

To begin, we perform a μ_3-acidity analysis on the CsCl-type phase. Ti in its elemental form is acidic, needing 1.80 electrons to achieve neutralization (represented with red hashed bars in Figure 4b). Cu, meanwhile, is basic with an excess of 5.05 electrons (blue hashed bars). Upon forming the CsCl structure, heteroatomic contacts are introduced, changing the μ_3 values of Ti and Cu. The shifts in μ_3 cause their BF_{ideal} values to move closer to their actual electron counts, diminishing their μ_3-

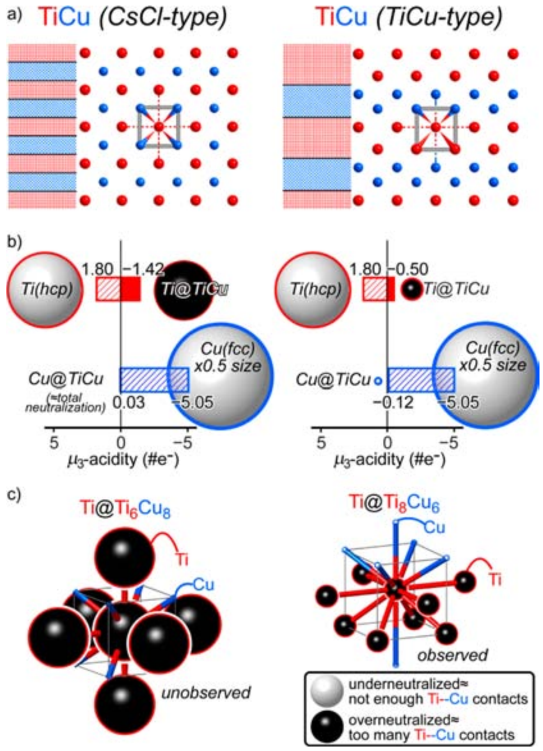

Figure 4. Structural origin of the enhanced μ_3-neutralization in the TiCu structure relative to the more common CsCl type. (a) The CsCl and TiCu type structures, viewed down the *a*-axis, alongside schematics of their Ti and Cu layers. (b) Bar graphs for the μ_3-neutralization calculated for the CsCl and TiCu structures. (c) Residual acidities (RAs) in the two structures represented as spheres overlaid on the Ti coordination environments. Underneutralized and overneutralized atoms are represented with white and black spheres, respectively, whose volumes are proportional to the magnitudes of their RAs. μ_3-acidic elements are outlined in red, μ_3-basic elements in blue. The scale of RA spheres is consistent throughout the figure.

acidity. For Cu in the CsCl-type, this results in almost complete neutralization. The Ti, on the other hand, shifts from acidic to basic, overshooting the neutral point by 1.42 electrons. We will refer to this situation where the change of the μ_3 overcompensates for the initial acidity or basicity as *overneutralization*.

As we look into how structure influences this neutralization, a visual representation of the μ_3-acidities/basicities will become important. We will use spheres overlaid on the atomic positions for this purpose. The color of each sphere corresponds to the manner in which the μ_3 is mismatched from the ideal value: Atoms that fall short of reaching the ideal from their original acidity/basicity (underneutralized) are plotted in white. Those that overshoot the ideal (overneutralized) are plotted in black. The sphere volumes indicate the magnitudes of the residual acidity (RA) on the atoms.

Ti and Cu in their elemental forms are represented with large white spheres, as they are thus far unreacted. With binary phase formation, the volumes of their representative spheres decrease along with the μ_3-acidity/basicity of the participating elements. The RA for Cu in the CsCl type all but disappears indicating nearly perfect neutralization of Cu, while the RA for Ti turns black as it crosses over the ideal to become overneutralized.

Using this graphical representation, the RA data can be related to structural features. In Figure 4c, we plot the RAs for the Ti coordination environment in the CsCl type. The central Ti atom appears with an inflated black RA sphere, surrounded by an octahedron of equally inflated Ti spheres. A cube of eight Cu atoms also surrounds the Ti atom, connected by bicolor red-blue cylinders. No spheres are visible at the ends of the bars connected to the Cu atoms due to Cu's high degree of neutralization here.

As neutralization is a function of heteroatomic contacts, the large black spheres on the Ti atoms express overexposure to the Cu atoms in the structure. A structural change reducing the number of Cu neighbors around the Ti would thus seem favorable. This is what is achieved by moving to the TiCu type. Doubling the Ti and Cu layers means that half of the Ti's eight Cu neighbors are replaced with Ti (Figure 4c), creating an aggregation of homoatomic bonding in the *ab*-plane. The composition of the coordination environment is then changed from 6 Ti and 8 Cu neighbors in the CsCl type to 8 Ti and 6 Cu in the TiCu-type. Qualitatively, we would expect this change to reduce the overneutralization of the Ti, as is indeed seen in the reduced size of the RA spheres on the Ti (Figure 4c, right).

The results for the previous section provide a path for making these considerations more quantitative. As we determined there, the largest contributing factors to the μ_3 are the relative strengths of hetero- and homoatomic bonding ($\mu_2^{\text{A-B}}/\mu_2$) and the size of the electronegativity difference relative to the spread in the distribution ($\Delta H_{ii}/\sigma$). Since the element types are the same in both structures, the H_{ii} parameters obtained for Ti and Cu are essentially constant (see Supporting Information). The change in μ_3-acidity must then come from another source, either σ or the $\mu_2^{\text{A-B}}/\mu_2$ ratio. The standard deviation between the two atoms' DOS distributions does differ slightly, but the larger difference between the two structures is in their $\mu_2^{\text{A-B}}$ to μ_2 ratios.

To see the effect of this parameter on the neutralization, let us look more closely at the calculation of the ideal electron count for Ti in the CsCl-type structure. We start by using eq 8 to calculate the μ_3 of the Ti atom:

$$\mu_{3,Ti} = \mu_{3,\text{Ti}}{}^{\text{A}-\text{B}} + \mu_{3,\text{Ti}}{}^{\text{triangle}} \approx \mu_{3,\text{Ti}}{}^{\text{A}-\text{B}}$$

$$\approx \left(\frac{\mu_2{}^{\text{A}-\text{B(eV)}}}{\mu_2{}^{\text{(eV)}}}\right)\left(\frac{\Delta H_{ii}{}^{\text{(eV)}}}{\sigma^{\text{(eV)}}}\right) = \left(\frac{0.753\text{ eV}}{1.31\text{ eV}}\right)\left(\frac{-4.16\text{ eV}}{1.14\text{ eV}}\right)$$

$$= -2.10$$

Using this μ_3 value, we then calculate the BF_{ideal} for the Ti atom:

$$\text{BF}_{\text{ideal,Ti}} = \frac{1}{2} + \frac{\mu_3}{2\sqrt{\mu_3^2 + 4}} = \frac{1}{2} + \frac{-2.10}{2\sqrt{(-2.10)^2 + 4}} = 0.138$$

As each Ti has a set of five d orbitals, this 13.8% ideal band-filling value corresponds to 1.38 electrons/Ti. The actual d-orbital population resulting from a DFT-calibrated Hückel calculation is 2.67 electrons/Ti, meaning that each Ti atom has as excess of 1.29 electrons over the ideal.

Upon going from the CsCl type to the TiCu type, the decrease in heteroatomic contacts lowers the $\mu_2^{\text{A-B}}/\mu_2$ ratio from 0.753 eV/1.31 eV to 0.495 eV/1.48 eV. To assess the effect of this change in the $\mu_2^{\text{A-B}}/\mu_2$ ratio, we can substitute the new ratio into the previous equation. Recalculating BF_{ideal} yields an ideal electron count of 2.40 electrons/Ti atom, which is much closer to the calculated occupancy for TiCu of 2.63 electrons. After substituting in all other factors associated with TiCu, the ideal becomes 2.13 electrons/atom.

From this calculation, we can see that the $\mu_2^{A\text{-}B}/\mu_2$ ratio has a strong enough influence over the total μ_3 to significantly improve the neutralization of the Ti atoms in the structure. This verifies that μ_3-neutralization of an atom is largely governed by the ratio of the aggregate heteroatomic bonding strength to the total aggregate bonding strength to its neighbors. These factors appear to be at work elsewhere in the Ti−Cu system as well: Ti_3Cu_4 and Ti_2Cu_3 have related structures also based on bcc packing.[66] In these structures the Ti and Cu similarly show a tendency to aggregate into double-layers, again reducing the opportunities for heteroatomic interactions.

So far we have focused on the Ti atoms of TiCu. What role does Cu have in the structural transition from CsCl to TiCu? Looking back at Figure 4, the μ_3-acidity analysis shows that Cu has little preference between the structures; it has a high degree of neutralization in both arrangements. At first it may seem odd that this structural change has such an asymmetrical influence on the Ti and Cu. In fact, the changes in the atomic μ_3 of the Ti and Cu atoms on going between the two structures are nearly equal and opposite. The differing impact on the μ_3-acidities of the two elements is connected to the functional relationship between μ_3 and BF (Figure 5).

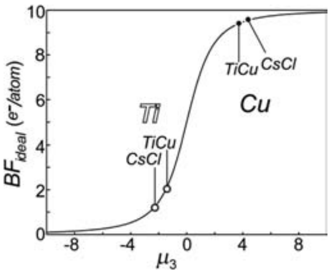

Figure 5. Functional relationship between μ_3 and the ideal BF of a DOS curve (as predicted for a μ_0−μ_4 model; see ref 41). The μ_3 values of each atom in the TiCu and CsCl structures are marked with dots.

The $BF_{ideal}(\mu_3)$ function has the shape of a titration curve, with relatively flat regions at the high and low μ_3 value ends, and a steep jump as μ_3 passes through 0. The ideal BF values, then, change very slowly at very negative μ_3 values, where the best occupancies are near 0, and very positive μ_3 values where the nearly filled levels are expected. The ideal BF is most sensitive in the range $-2 \leq \mu_3 \leq 2$, where intermediate BF values are predicted. This means that a small change in μ_3 within the −2 to 2 range will yield a large change in the BF_{ideal}. Since the Ti μ_3 values rest within or close to this range, slight changes in the μ_3 from the structure have a significant effect on the BF_{ideal}. Cu is situated higher in the μ_3 range, which makes small changes to the μ_3 have weaker effects on the BF_{ideal}. The lowered bonding preferences of Cu are a consequence of the atom's almost completely populated energy levels.

In summary, the optimization of μ_3-neutralization through changes in local coordination drives the thicker atomic layers in the TiCu-type structure; homoatomic contacts offered by this structure type assuage overneutralization of the Ti. The structural shift also causes Cu to take on more Cu neighbors, but Cu is buffered by its large μ_3 value, preventing instability.[67] In the next section, we will see how other structural motifs can arise in a compound's search for μ_3-neutrality.

■ The $Ti_{21}Mn_{25}$ STRUCTURE

As we saw in the previous section, when Ti is paired with Cu in the CsCl structure, Cu is too strong of a base and overneutralizes the Ti atoms. If we replace Cu with a very weak base, such as Mn, however, a similar problem emerges. The pairing of Ti and Mn in a CsCl-type phase produces overneutralization, this time not on the Ti, but on the Mn. This is illustrated in Figure 6b for the Mn coordination geometry.

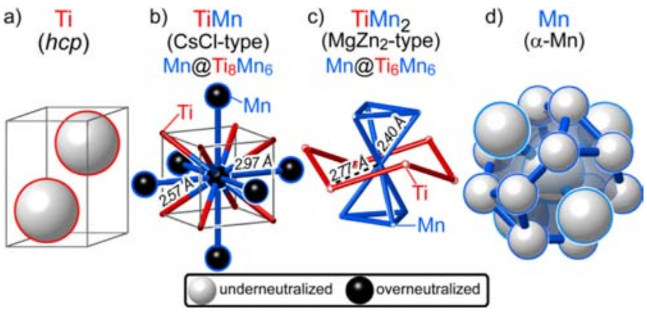

Figure 6. Residual acidities (RAs) of observed and hypothetical phases across the Ti−Mn phase diagram. (a) Elemental hcp Ti. (b) A hypothetical CsCl-type TiMn phase. (c) The observed $MgZn_2$-type $TiMn_2$. (d) Elemental Mn (α-form). For panels b−d, each structure is illustrated with the coordination environment of one of its Mn atoms.

The Mn atoms exhibit relatively large, black RA spheres, while the surrounding Ti atoms are close to neutral. The large RAs indicate that Mn is overexposed to Ti. This might be anticipated from its coordination environment. Mn connects with more Ti than Mn atoms (8Ti + 6Mn), and the Ti contacts are closer than the Mn ones. To alleviate the exposure, one could replace Ti with a weaker acid, such as V, which does indeed form a CsCl-type phase with Mn.

Another way to reduce overneutralization of the Mn by Ti would be to dilute the Ti−Mn interactions through the introduction of more Mn. In fact, every intermetallic phase in the Ti−Mn phase diagram [$Ti_{49.5}Mn_{50.5}$, $Ti_{21}Mn_{25}$, $TiMn_2$, $TiMn_3$ (high-temperature), Ti_9Mn_{42} (high-temperature)] lies to the Mn-rich side of the 1:1 composition.[68] The extra Mn would be expected to increase the number of Mn−Mn contacts, protecting Mn from the Ti.

Such is found in the structure of $TiMn_2$. $TiMn_2$ adopts the $MgZn_2$ type (Figure 7a), in which Ti atoms form a hexagonal diamond framework, threading through a network of face sharing Mn truncated tetrahedra. Here the Mn occupies icosahedral coordination polyhedra (Figure 6c), consisting of 6 Ti and 6 Mn atoms, as opposed to 8 Ti and 6 Mn in the CsCl type. The heteroatomic/homoatomic bond distance ratio also inverts, such that the Mn−Mn contacts are now shorter than the Ti−Mn contacts (2.40 Å compared to 2.77 Å).[69] As expected, the Mn RAs are much lower here than in the CsCl-type (Figure 6c).

Just as in the TiCu example, the influence of the geometry of the Ti−Mn phases on μ_3-neutralization can be explored with the $\mu_2^{A\text{-}B}/\mu_2$ ratio. Since our focus is on the Mn sites in these two structures, we can rewrite $\mu_2^{A\text{-}B}/\mu_2$ as $[(\mu_2^{Mn-Ti})/(\mu_2^{Mn-Ti} + \mu_2^{Mn-Mn})]$. When this ratio approaches unity, the strength of homoatomic bonding is very small compared to the strength of

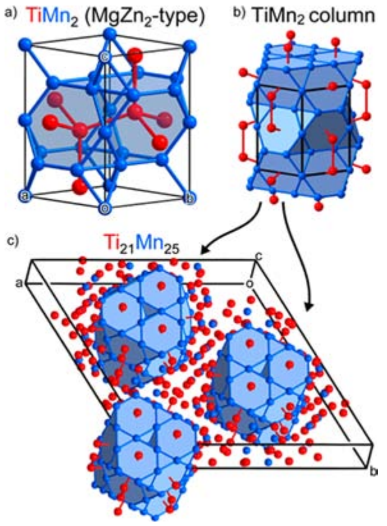

Figure 7. MgZn$_2$-type TiMn$_2$ and its role in the Ti$_{21}$Mn$_{25}$ crystal structure. (a) The TiMn$_2$ structure. (b) A column of the TiMn$_2$ structure, for comparison with Ti$_{21}$Mn$_{25}$. (c) The Ti$_{21}$Mn$_{25}$ unit cell, in which a large fraction of the space is filled by TiMn$_2$ columns; the remainder can be viewed as a Ti-rich matrix.

heteroatomic bonding. For Mn in the CsCl-type, the $\mu_2^{\text{A-B}}/\mu_2$ value is 0.87, indicating that Mn−Mn bonding has little influence on the μ_3 of the Mn atoms. The TiMn$_2$ structure shifts this balance significantly. Mn−Mn contacts are shorter, and in response, the $\mu_2^{\text{Mn−Mn}}$ increases from 0.27 eV in the CsCl type to an average value of 1.57 eV among the Mn sites in TiMn$_2$. In TiMn$_2$, Mn's fewer Ti neighbors and longer Ti−Mn distances lead to a reduction in $\mu_2^{\text{Mn−Ti}}$ by over 50%. These geometrical changes work simultaneously to decrease the $\mu_2^{\text{A-B}}/\mu_2$ to 0.33. The overall Mn μ_3 is then reduced, which lowers the BF$_{\text{ideal}}$ to be more consistent with the actual Mn d-orbital occupancy.

Given the nearly ideal neutralization experienced in the MgZn$_2$-type TiMn$_2$, it is understandable that its geometrical features might be retained in phases with other compositions. This is the case in Ti$_{21}$Mn$_{25}$. In the Ti$_{21}$Mn$_{25}$ structure, columns of the TiMn$_2$ structure are present. The columns are arranged in a hexagonal rod packing to form a rhombohedral cell (Figure 7c). The additional Ti atoms which bring the phase to a near 1:1 composition are concentrated in the spaces between the TiMn$_2$ columns. In other words, it appears that a 1:1 TiMn reaction mixture disproportionated upon crystallization into small domains of TiMn$_2$ and a Ti-rich matrix.

In Figure 8, we compare the distribution of RAs within TiMn$_2$ and Ti$_{21}$Mn$_{25}$ to evaluate how well this view of the Ti$_{21}$Mn$_{25}$ structure is reflected in a μ_3-acidity analysis. In Figure 8a, we show a large section of the TiMn$_2$ structure looking down the *c*-axis. This section can be thought of as a precursor to the Ti$_{21}$Mn$_{25}$ structure before fragmentation and intercalation of Ti atoms between the fragments. To emphasize this perspective, the Mn−Mn are drawn, and the precursors to the columns in Ti$_{21}$Mn$_{25}$ are highlighted in sky blue. Because the TiMn$_2$ is a bulk phase and not actually fragmented into columns, some Mn and Ti atoms are shared at the boundaries between columns.

Within the distribution of RAs in the Ti$_{21}$Mn$_{25}$ unit cell (Figure 8b), two types of regions are apparent: one exhibiting small RA spheres in pockets throughout the structure, and honeycomb shaped domains of larger RA spheres surrounding the regions of the first type. Comparing the location of the TiMn$_2$ columns (sky blue) to the distribution of RA spheres reveals that the regions of high neutralization coincide with these columns. The MgZn$_2$-type features continue to facilitate neutrality, even when embedded in the more complex crystal structure of Ti$_{21}$Mn$_{25}$. The less neutralized section is mostly made up of relatively large white spheres in red outline, indicating a prevalence of Ti.

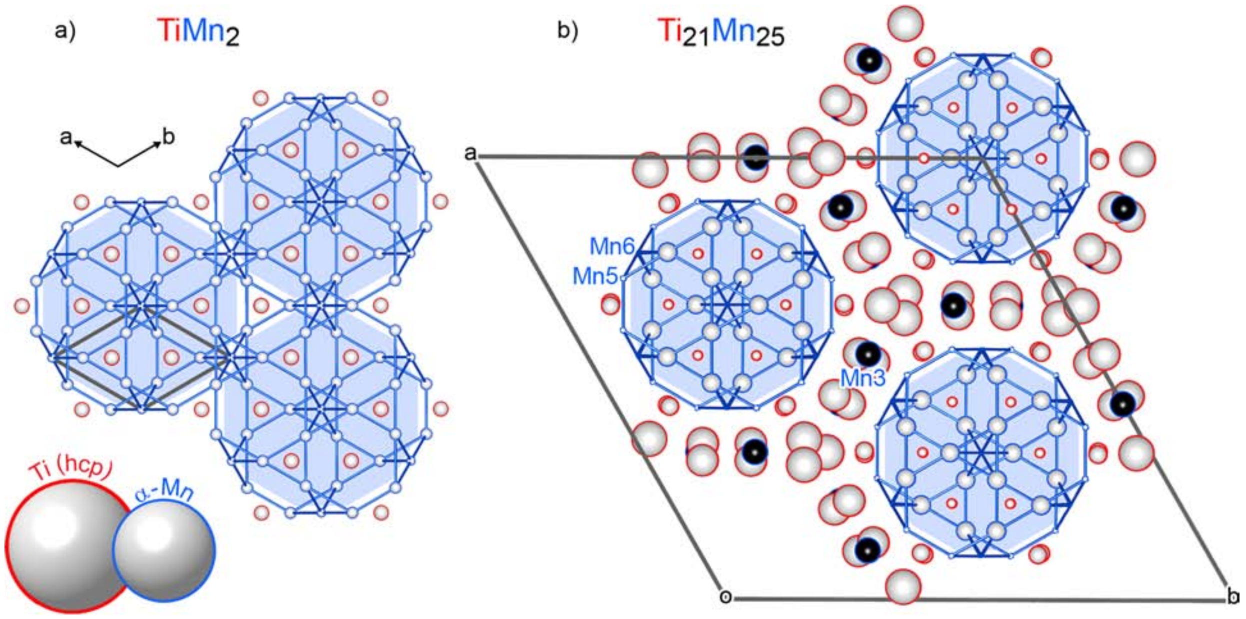

Figure 8. Quantum mechanical view of the TiMn$_2$ and Ti$_{21}$Mn$_{25}$ structures using residual acidities (RAs). The RAs for elemental Ti and Mn are shown in the bottom left for comparison. For plotting conventions, see the caption to Figure 4. The volume of the RA spheres are inflated relative to those of Figure 6 to make the RA distributions clearly visible. The locations of the corresponding TiMn$_2$ columns in each structure are emphasized with Mn−Mn bonds of the truncated tetrahedral network drawn in blue and additionally highlighted with a light blue background.

By comparing the μ_3-acidity results for $TiMn_2$ and $Ti_{21}Mn_{25}$, we note that the fragmentation of the $TiMn_2$ structure creates a change in the distribution of the RAs on the $TiMn_2$ columns. For example certain sites on the perimeter (Mn5, Mn6) and very center (Mn1) of the $TiMn_2$ fragments within $Ti_{21}Mn_{25}$ are particularly well-neutralized. Their residual acidity is so small that no spheres are visible in the plot. The unusually well neutralized sites on the exterior of the $TiMn_2$ fragments, Mn5 and Mn6, provide an important indication as to why the fragmentation of $TiMn_2$ is favorable. Numerically, Mn5 and Mn6 sites exhibit residual acidities of −0.07 and −0.03 electrons, respectively. The analogous sites in the bulk $TiMn_2$ phase clearly do not reach the same level of neutralization. The heightened neutralization at the surface of the $TiMn_2$ fragments could provide a sizable driving force for interface formation. While some sites in $Ti_{21}Mn_{25}$ have slightly greater RAs than their analogues in the $TiMn_2$ structure, the highly neutralized sites make up a majority of the Mn sites (52%), outweighing the increase in RA at other sites.

The poorer neutralization within $TiMn_2$ on the sites analogous to Mn5 and Mn6 indicates a slight excess in homoatomic interactions relative to heteroatomic ones. In the bulk $TiMn_2$ sites, all Mn atoms have a Ti:Mn neighbor ratio of 6:6. Fragmenting the $TiMn_2$ structure within $Ti_{21}Mn_{25}$ breaks the Mn−Mn network and stuffs Ti atoms between the fragments. For these outer sites, these actions translate into losing Mn neighbors and gaining Ti ones, causing the Mn5 and Mn6 neighbor ratios to become 5 Mn:7 Ti. Part of this coordination includes contacts to an additional Mn site (Mn3) between the $TiMn_2$ fragments. Due to their placement middle of the Ti-rich region, the Mn3 sites are slightly overneutralized (0.33 electrons), as is evident from their black RA spheres in Figure 8b. At first, this would seem to be destabilizing, but these sites only make up a minority of the structure's Mn atoms (12%). For the more prevalent Mn5 and Mn6 atoms, the fragmentation delivers just the right nearest neighbor ratio to remove the last vestiges of acidity.

The changed Ti:Mn neighbor ratio at the fragment interface, along with some adjustments in the interatomic distances,[70] is reflected in the $\mu_2^{\text{A-B}}/\mu_2$ of the sites at the interface. In $TiMn_2$, the sites corresponding to Mn5 and Mn6 have $\mu_2^{\text{Mn−-Ti}}/\mu_2$ values of 0.37 and 0.33. From increasing the Mn−Ti interaction strength and decreasing the Mn−Mn strength, the Mn5 and Mn6 sites' $\mu_2^{\text{Mn−Ti}}/\mu_2$ ratios increase to 0.40 and 0.41, respectively. This increase serves to raise the BF_{ideal} just enough to remove the remaining basicity on the Mn atoms.

The remainder of the structure is made up of the excess Ti that intercalates between the $TiMn_2$ fragments. The excess Ti represents an interesting puzzle. So far, we've established that creating a balance between homoatomic and heteroatomic bonding promotes neutralization within intermetallic structures. We might expect that an aggregated excess of a particular element, as with the Ti here, would create μ_3-acidity values near those of the elemental form, making macroscopic phase segregation a possibility. However, by comparing the RAs of elemental Ti (lower left of Figure 8a) with the RAs of the $Ti_{21}Mn_{25}$ structure (Figure 8b), we see that the Ti atoms in fact experience considerable neutralization in the $Ti_{21}Mn_{25}$ structure. Each Ti site between the $TiMn_2$ fragments of the $Ti_{21}Mn_{25}$ structure displays at least a 5-fold reduction in its RA relative to elemental Ti.

To understand how this neutralization occurs, let us examine more closely the Ti-rich domain in $Ti_{21}Mn_{25}$. A look at the surroundings of the Ti atoms between the $TiMn_2$ fragments reveals that these atoms arrange into a distorted version of stella quadrangula (SQ), a common structural motif in intermetallics (Figure 9a). SQ are compound polyhedra formed by fusing five tetrahedra together, with a central tetrahedron sharing each of its faces with an outer tetrahedron. These structures are archetypal of tetrahedral close packing (tcp), the packing mode underlying the $TiMn_2$ structure and most of the $Ti_{21}Mn_{25}$ structure. The Ti-rich matrix surrounding the $TiMn_2$ fragments, however, exhibits a severely distorted version of this packing. The distortion, displayed in the center of Figure 9a, stretches the SQ to break up the contacts building up the central tetrahedron. This motion reduces the density of Ti−Ti contacts, so much so that rotating the distorted SQ (Figure 9a, right) reveals a square-shaped opening through the polyhedron.

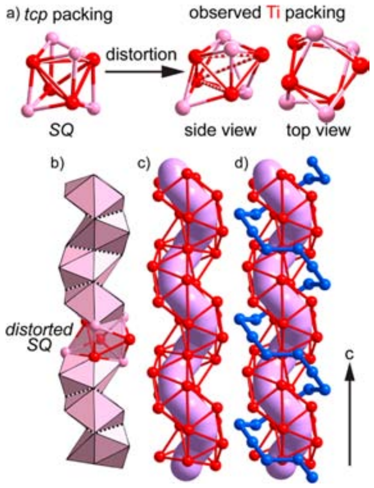

Figure 9. Helical tubes arising in the Ti-rich region of $Ti_{21}Mn_{25}$ through the opening of squares in a tetrahedral close-packing. (a) Ti atoms arrange in a distorted stella quadrangula (SQ), in which openings occur at the top and bottom of the polyhedra. (b) These polyhedra stack through shared faces along the *c*-axis. (c) Connecting the Ti atoms shows that the Ti contacts trace out a Ti triangular net which encapsulates an empty space (represented in purple), traveling in a helix along the *c*-axis. (d) The helical tube of Ti atoms is wrapped by an interlocking helix of Mn atoms, forming a double-helical arrangement.

The distorted SQ are stacked along *c*, through shared faces (Figure 9b). This stacking aligns the openings of the distorted polyhedra to form a continuous empty channel of Ti atoms (Figure 9c). The diameter of the channel is about 2.6 Å, with the shortest Ti−Ti contacts between walls being 3.70−4.15 Å. In Figure 9c, the space between the walls of the channel is emphasized with a purple tube. Here an intriguing feature of the structure becomes apparent: the openings align with a twist, creating a helix along the *c*-axis.

μ_3-Acidity analysis offers a concise explanation for the presence of these empty channels. We begin by considering a return to undistorted SQ, closing up the channel to recover a tetrahedral packing of Ti. This undistortion of the Ti helical tube would add 4, 2, and 2 neighbors to the coordination spheres of the Ti1, Ti2, and Ti4 sites of the helix, respectively. In the language of moments, the increase in close Ti neighbors means an increase in the homoatomic μ_2 component. The addition of these homoatomic contacts is estimated[71] to increase the underneutralization of the Ti atoms by 0.16 to 0.28

electrons/atom. This brings the newly tetrahedrally packed sites to a residual acidity ranging from 1.0 to 1.3 electrons, offering reduced improvements on the original acidity of elemental Ti (1.8 electrons). By opening up the tighter tcp structure, the Ti assumes a sparser packing to diminish the $\mu_2^{\text{Ti-Ti}}$ of the helical sites. Decreasing the density of homoatomic bonding in this way influences the potential for Mn atoms to neutralize the Ti. The lowered $\mu_2^{\text{Ti-Ti}}$ values decrease the dominator of $\mu_2^{\text{A-B}}/\mu_2$ which enhances the impact of the few Ti−Mn contacts involving these excess Ti atoms.

The channel formed from the excess Ti atoms thus helps to enhance overneutralization. The twist which creates the helix, however, has yet to be explained. A clue within the structure is provided: a thread of Mn atoms wraps around the Ti helix, nestling into the groove of the helix (Figure 9d). These Mn atoms form an additional helix that rotates in the same direction as the Ti helix (just like the two polymers of nucleotides in DNA).

To see if the twist of the helix provides anything important to the bonding within this section of the $Ti_{21}Mn_{25}$ structure, we can consider an alternative structure without a twist. In Figure 10a, we show a column of Ti with its walls made up of a triangular net of Ti atoms as in the walls of the helix. Since there is a scarcity of Mn atoms in the Ti-rich section of $Ti_{21}Mn_{25}$, it is expected that the Mn atoms would try to situate where they would create the most Mn−Ti contacts to neutralize the Ti. In the case of the column, Mn could coordinate in two possible ways to maximize its bonding to the column: at the center of a Ti triangle or at an edge shared by two triangles.

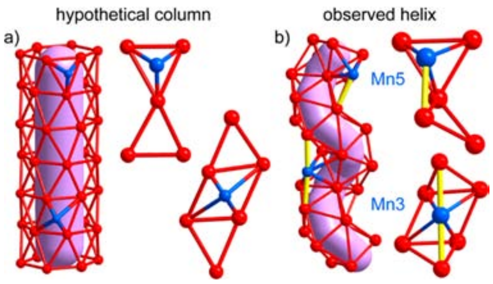

Figure 10. Advantages of the Ti helical tube geometry over a straight column for maximizing Ti−Mn interactions in the Ti-rich matrix of $Ti_{21}Mn_{25}$. (a) Possible Mn sites on a hypothetical Ti column, derived from a triangular net wrapped into a tube. (b) The docking sites for Mn in the observed helical Ti structures of the $Ti_{21}Mn_{25}$ structure. The concavity offered by the groove of the observed helix provides more Ti−Mn contacts (yellow) than the corresponding sites on the column.

In Figure 10, we compare this coordination with what is seen on the helical tube of the $Ti_{21}Mn_{25}$ structure. If we focus on the coordination of the two Mn sites that lie in the groove of the Ti helix, we see that their placement on the helix resembles those on the hypothetical column: Mn is either capping a triangle (Mn5) or a diamond (Mn3) of Ti atoms. However, the twist in the helix imparts concavity to the Ti net. The concave surface of the helix increases the surface area to provide the Mn with additional Ti contacts. The Mn5 site not only caps a triangle but the twist moves a Ti atom that was once in the plane of the triangle to bend inward toward the Mn. The Mn3 site, which caps a diamond of Ti takes on two more neighbors as the Ti atoms above and below the diamond bend to form the groove of the helix.

In effect, the manifestation of Ti helices reflects the same need for balance in homoatomic/heteroatomic interactions seen throughout this Article. Since Mn atoms are in short supply in this domain, adopting an open homoatomic structure readies the Ti to be more susceptible to Mn changing its μ_3 value. Adding helicity to this structure then creates more opportunities for heteroatomic bonding to occur. The helices illustrate how crystal structure can play an active role in μ_3-neutralization.

The two dominant structural themes in $Ti_{21}Mn_{25}$, the $TiMn_2$ column and the Ti−Mn double helix, account for all of the atoms in the structure. Through our μ_3-acidity analysis, a simple story of this structure's origin comes into focus. We envision a hypothetical 1:1 CsCl-type phase disproportionating into sections of the $TiMn_2$ structure and excess Ti, ensuring a large amount of Mn−Mn connectivity to avoid overneutralization of the Mn atoms. The $TiMn_2$ structure, however, is not perfect. The Mn atoms within the $TiMn_2$ structure could be better neutralized if they were bonded to fewer Mn atoms and more Ti atoms. The $TiMn_2$ structure then splits apart to break the Mn−Mn network, inviting Ti atoms to intercalate. As the Ti arranges around the fragments, it adopts the hollow helical structure to maximize the neutralizing effect of the available Mn neighbors in the structure.

■ CONCLUSIONS

Over the history of chemistry, Acidity has been a rich and mercurial notion, whose evolution traces the growth of theoretical models to account for an increasingly broad range of empirical observations of reactivity. This is well illustrated in the familiar progression from the Arrhenius definition,[72] with its focus on the reactions of H^+ and OH^-, through the Brønsted−Lowry model,[73,74] to Lewis's acid−base theory which recognizes any transaction involving electron pair donation and acceptance as a neutralization reaction,[75,76] and onward to Pearson's concept of hard and soft acids and bases.[77] And still the idea of acidity continues to acquire new facets. By shifting the focus to the atom's electron excess or deficiency relative to its ideal count, we have seen that the μ_3-acidity model extends the language of acidity as far as understanding the stability and structures of intermetallic phases based on transition metals.

Whatever the wisdom of this endeavor, we have arrived at a means of understanding some of the beautiful structural motifs observed in intermetallics. The μ_3-acidity of a metal atom is strongly tied to the composition of its first coordination sphere, with the balance of heteroatomic and homoatomic contacts determining the extent of neutralization provided by the reaction of μ_3-acidic and basic metals. In TiCu and $Ti_{21}Mn_{25}$, we saw a number of examples demonstrating how structural motifs are adopted to achieve this balance for optimal neutralization. In the crystal structure of TiCu, the insertion of antiphase boundaries in the CsCl type serves to protect the Ti from overneutralization by the Cu. More striking structural rearrangements are seen in $Ti_{21}Mn_{25}$ to shield the weak μ_3-base Mn from the relatively strong μ_3-acid Ti. The structure segregates at the nanometer scale into Ti-poor $MgZn_2$-type domains and a Ti-rich matrix. The Ti-rich matrix atoms adopt a helical tube geometry which allows them to gain the maximal neutralization possible from their few Mn neighbors.

The explanation of the $Ti_{21}Mn_{25}$ structure in terms of μ_3-neutralization has implications for understanding some of the most complex intermetallic structures solved to date: Samson's classic structures of $NaCd_2$,[78] Mg_2Al_3,[79] and Cd_3Cu_4,[80] whose giant cubic unit cells contain more than 1000 atoms. These structures share with $Ti_{21}Mn_{25}$ the feature of containing large fragments of Laves phase structures. In fact, such Laves phase fragments have been recognized in a growing body of compounds, including the breath-taking structures of $Al_{56.5}Cu_{3.9}Ta_{39.5}$ (*cF*5,908) and $Al_{55.4}Cu_{5.4}Ta_{39.1}$ (*cF*23,134) recently determined by Harbrecht, Steurer, and co-workers.[81,82]

Our comparison of the residual acidities for the $MgZn_2$-type columns in $Ti_{21}Mn_{25}$ and the $MgZn_2$-type $TiMn_2$ illustrates that these Laves fragments are an electronically important geometrical component of the structure. This confirms an earlier result based on Mulliken population analysis of the $Mg_{17}Al_{12}$ and $NaCd_2$ structures.[83] The use of μ_3-acidity, however, begins to go beyond identifying such geometrical entities toward explaining the origins of the fragmentation of the Laves phases in these structures. It will be interesting to determine the role that acid/base strengths play in the structural chemistry of Laves phase variants as a whole. The μ-phase structure of Co_7Mo_6,[84] with its alternating Laves and μ-phase polyhedra layers, provides one starting point for this more general investigation.

We suspect that more of the structural diversity of intermetallics can be explained in this way and are looking forward to applying this analysis to additional complex intermetallics. The roots of μ_3-acidity in the Method of Moments also mean that, in principle, it should be applicable beyond crystalline phases to analyzing bonding and reactivity in systems such as defects, surfaces, edges, or nanostructured materials. However, challenges remain. To be generally useful, these concepts will need to be extended beyond the d-block elements. Additionally, μ_3-neutralization represents only one of several driving forces determining intermetallic structures, including size effects (as might be understood from DFT-CP analysis[85]) and electronic interactions in k-space as described by the Mott–Jones model.[86] The integration of all these factors into a coherent conceptual framework for intermetallics is an exciting long-term prospect of sustained exploration of their bonding and electronic structure.

■ ASSOCIATED CONTENT

Ⓢ Supporting Information

Details of the DFT computational procedures. Coordinates and total energies of the optimized structures. Tables of DFT-calibrated Hückel parameters. This material is available free of charge via the Internet at http://pubs.acs.org.

■ AUTHOR INFORMATION

Corresponding Author

*E-mail: danny@chem.wisc.edu.

Notes

The authors declare no competing financial interest.

■ ACKNOWLEDGMENTS

We gratefully acknowledge the financial support of the U.S. DOE office of Science Early Career Program (DE-SC0003947) through the Office of Basic Energy Sciences, and the University of Wisconsin through start-up funds. This research involved calculations using computer resources supported by National Science Foundation Grant CHE-0840494.

■ REFERENCES

(1) Snyder, G. J.; Toberer, E. S. *Nat. Mater.* **2008**, *7*, 105–114.

(2) Quarez, E.; Hsu, K.-F.; Pcionek, R.; Frangis, N.; Polychroniadis, E. K.; Kanatzidis, M. G. *J. Am. Chem. Soc.* **2005**, *127*, 9177–9190.

(3) Androulakis, J.; Todorov, I.; He, J.; Chung, D.-Y.; Dravid, V.; Kanatzidis, M. *J. Am. Chem. Soc.* **2011**, *133*, 10920–10927.

(4) Kovalenko, M. V.; Spokoyny, B.; Lee, J.-S.; Scheele, M.; Weber, A.; Perera, S.; Landry, D.; Talapin, D. V. *J. Am. Chem. Soc.* **2010**, *132*, 6686–6695.

(5) Joshi, G.; Lee, H.; Lan, Y.; Wang, X.; Zhu, G.; Wang, D.; Gould, R. W.; Cuff, D. C.; Tang, M. Y.; Dresselhaus, M. S.; Chen, G.; Ren, Z. *Nano Lett.* **2008**, *8*, 4670–4674.

(6) Higgins, J. M.; Schmitt, A. L.; Guzei, I. A.; Jin, S. *J. Am. Chem. Soc.* **2008**, *130*, 16086–16094.

(7) Aricò, A. S.; Bruce, P.; Scrosati, B.; Tarascon, J.-M.; Van Schalkwijk, W. *Nat. Mater.* **2005**, *4*, 366–377.

(8) Williams, M.; Lototsky, M. V.; Linkov, V. M.; Nechaev, A. N.; Solberg, J. K.; Yartys, V. A. *Int. J. Energy Res.* **2009**, *33*, 1171–1179.

(9) Wang, X.-L.; Han, W.-Q.; Chen, J.; Graetz, J. *ACS Appl. Mater. Interfaces* **2010**, *2*, 1548–1551.

(10) Wang, X.-L.; Feygenson, M.; Chen, H.; Lin, C.-H.; Ku, W.; Bai, J.; Aronson, M. C.; Tyson, T. A.; Han, W.-Q. *J. Am. Chem. Soc.* **2011**, *133*, 11213–11219.

(11) Androulakis, J.; Lin, C.-H.; Kong, H.-J.; Uher, C.; Wu, C.-I.; Hogan, T.; Cook, B. A.; Caillat, T.; Paraskevopoulos, K. M.; Kanatzidis, M. G. *J. Am. Chem. Soc.* **2007**, *129*, 9780–9788.

(12) Armbrüster, M.; Kovnir, K.; Behrens, M.; Teschner, D.; Grin, Y.; Schlögl, R. *J. Am. Chem. Soc.* **2010**, *132*, 14745–14747.

(13) Ghosh, T.; Vukmirovic, M. B.; DiSalvo, F. J.; Adzic, R. R. *J. Am. Chem. Soc.* **2010**, *132*, 906–907.

(14) Qiao, Y.; Li, C. M. *J. Mater. Chem.* **2011**, *21*, 4027.

(15) Kang, Y.; Pyo, J. B.; Ye, X.; Gordon, T. R.; Murray, C. B. *ACS Nano* **2012**, *6*, 5642–5647.

(16) Alden, L. R.; Roychowdhury, C.; Matsumoto, F.; Han, D. K.; Zeldovich, V. B.; Abruña, H. D.; DiSalvo, F. J. *Langmuir* **2006**, *22*, 10465–10471.

(17) Kim, J.; Lee, Y.; Sun, S. *J. Am. Chem. Soc.* **2010**, *132*, 4996–4997.

(18) Maksimuk, S.; Yang, S.; Peng, Z.; Yang, H. *J. Am. Chem. Soc.* **2007**, *129*, 8684–8685.

(19) Xia, B. Y.; Wu, H. B.; Wang, X.; Lou, X. W. *J. Am. Chem. Soc.* **2012**, *134*, 13934–13937.

(20) Kang, Y.; Murray, C. B. *J. Am. Chem. Soc.* **2010**, *132*, 7568–7569.

(21) Kang, Y.; Qi, L.; Li, M.; Diaz, R. E.; Su, D.; Adzic, R. R.; Stach, E.; Li, J.; Murray, C. B. *ACS Nano* **2012**, *6*, 2818–2825.

(22) Armbrüster, M.; Kovnir, K.; Friedrich, M.; Teschner, D.; Wowsnick, G.; Hahne, M.; Gille, P.; Szentmiklósi, L.; Feuerbacher, M.; Heggen, M.; Girgsdies, F.; Rosenthal, D.; Schlögl, R.; Grin, Y. *Nat. Mater.* **2012**, *11*, 690–693.

(23) Casado-Rivera, E.; Volpe, D. J.; Alden, L.; Lind, C.; Downie, C.; Vázquez-Alvarez, T.; Angelo, A. C. D.; DiSalvo, F. J.; Abruña, H. D. *J. Am. Chem. Soc.* **2004**, *126*, 4043–4049.

(24) Prinz, J.; Gaspari, R.; Pignedoli, C. A.; Vogt, J.; Gille, P.; Armbrüster, M.; Brune, H.; Gröning, O.; Passerone, D.; Widmer, R. *Angew. Chem., Int. Ed.* **2012**, *51*, 9339–9343.

(25) Andersson, M. P.; Bligaard, T.; Kustov, A.; Larsen, K. E.; Greeley, J.; Johannessen, T.; Christensen, C. H.; Nørskov, J. K. *J. Catal.* **2006**, *239*, 501–506.

(26) Hughbanks, T.; Hoffmann, R. *J. Am. Chem. Soc.* **1983**, *105*, 1150–1162.

(27) Hughbanks, T.; Hoffmann, R. *J. Am. Chem. Soc.* **1983**, *105*, 3528–3537.

(28) Dronskowski, R.; Bloechl, P. E. *J. Phys. Chem.* **1993**, *97*, 8617–8624.

(29) Becke, A. D.; Edgecombe, K. E. *J. Chem. Phys.* **1990**, *92*, 5397–5403.

(30) Savin, A.; Becke, A. D.; Flad, J.; Nesper, R.; Preuss, H.; von Schnering, H. G. *Angew. Chem., Int. Ed.* **1991**, *30*, 409–412.

(31) Savin, A.; Nesper, R.; Wengert, S.; Fässler, T. F. *Angew. Chem., Int. Ed.* **1997**, *36*, 1808−1832.

(32) Kohout, M. *Int. J. Quantum Chem.* **2004**, *97*, 651−658.

(33) Kohout, M.; Pernal, K.; Wagner, F. R.; Grin, Y. *Theor. Chem. Acc.* **2004**, *112*, 453−459.

(34) Kohout, M.; Pernal, K.; Wagner, F. R.; Grin, Y. *Theor. Chem. Acc.* **2005**, *113*, 287−293.

(35) Kohout, M.; Wagner, F. R.; Grin, Y. *Theor. Chem. Acc.* **2008**, *119*, 413−420.

(36) *Chemistry, Structure, and Bonding of Zintl Phases and Ions: Selected Topics and Recent Advances*, 1st ed.; Kauzlarich, S. M., Ed.; Wiley-VCH: New York, 1996.

(37) Sevov, S. C. In *Intermetallic Compounds—Principles and Practice*; Westbrook, J. H., Fleischer, R. L., Eds.; John Wiley & Sons, Ltd: Chichester, U.K., 2002; pp 113−132.

(38) *Zintl Phases: Principles and Recent Developments*; Fässler, T. F., Ed.; Springer: Berlin, 2011.

(39) Brewer, L.; Wengert, P. R. *Metall. Trans. B* **1973**, *4*, 83−104.

(40) Dronskowski, R. *J. Am. Chem. Soc.* **1992**, *114*, 7230−7244.

(41) Stacey, T. E.; Fredrickson, D. C. *Inorg. Chem.* **2012**, *51*, 4250−4264.

(42) Drago, R. S.; Wayland, B. B. *J. Am. Chem. Soc.* **1965**, *87*, 3571−3577.

(43) Since the publication of ref 41, we have realized that the original definition of μ_3-acidity as the actual electron count minus the ideal is a little counterintuitive: acidic atoms end up with negative μ_3-acidity values. In this Article, and in ref 56, we have included a factor of −1 to correct this. For this reason, the *x*- and *y*-axis values in Figure 1 differ from those in ref 41 by a sign change.

(44) Additional non-CsCl-type 1:1 phases include $V_{0.5}Fe_{0.5}$ in the σ-type phase: Van der Kraan, A. M.; Buschow, K. H. J. *Physica B & C* **1986**, *138*, 55−62. $Mn_{0.5}Co_{0.5}$ in the *fcc*-type: Karlsen, O. B.; Kjekshus, A.; Fjellvåg, H.; Ravindran, P.; Vidya, R.; Hauback, B. C. *J. Alloys Compd.* **2009**, *476*, 9−13. MnNi in the AuCu-type: Buschow, K. H. J.; van Engen, P. G.; Jongebreur, R. *J. Magn. Magn. Mater.* **1983**, *38*, 1−22. MnNi also adopts the CsCl-type but only at high temperatures: Egorushkin, V. E.; Kulkov, S. N.; Kulkova, S. E. *Physica B+C* **1983**, *123*, 61−68.

(45) Karlsson, N. *J. Inst. Met.* **1951**, *79*, 391−405.

(46) There are also reports of a 1:1 σ-type phase occurring in the TiMn system. One is the identification of such a phase from powder data in the 1950s: Elliott, R. P.; Rostoker, W. *Trans. AIME* **1953**, *197*, 1203−1204. Another lists it as a component in multiphase regions of the Ti−Mn−Sb system: Tkachuk, A.; Gorelenko, Yu.; Stadnyk, Yu.; Padlyak, B.; Jankowska-Frydel, A.; Bodak, O.; Sechovsky, V. *J. Alloys Compd.* **2001**, *319*, 74−79. However, none of the binary phase Ti−Mn diagrams of which we are aware, some very recent, show indications of such a compound. We are currently undergoing our own synthetic investigations in this portion of the Ti−Mn system.

(47) Cenzual, K.; Parthé, E.; Waterstrat, R. M. *Acta Crystallogr., Sect. C* **1986**, *42*, 261−266.

(48) Kresse, G.; Hafner, J. *Phys. Rev. B* **1993**, *47*, 558.

(49) Kresse, G.; Hafner, J. *Phys. Rev. B* **1994**, *49*, 14251.

(50) Kresse, G.; Furthmüller, J. *Comput. Mater. Sci.* **1996**, *6*, 15.

(51) Kresse, G.; Furthmüller, J. *Phys. Rev. B* **1996**, *54*, 11169.

(52) Perdew, J. P.; Chevary, J. A.; Vosko, S. H.; Jackson, K. A.; Pederson, M. R.; Singh, D. J.; Fiolhais, C. *Phys. Rev. B* **1992**, *46*, 6671.

(53) Perdew, J. P.; Chevary, J. A.; Vosko, S. H.; Jackson, K. A.; Pederson, M. R.; Singh, D. J.; Fiolhais, C. *Phys. Rev. B* **1993**, *48*, 4978.

(54) Blöchl, P. E. *Phys. Rev. B* **1994**, *50*, 17953.

(55) Kresse, G.; Joubert, D. *Phys. Rev. B* **1999**, *59*, 1758.

(56) Stacey, T. E.; Fredrickson, D. C. *Dalton Trans.* **2012**, *41*, 7801−7813.

(57) Landrum, G.; Glassey, W. *YAeHMOP: Yet Another extended Hückel Molecular Orbital Package, Version 3.0.* The YAeHMOP software is freely available on the web at http://sourceforge.net/projects/yaehmop.

(58) Cyrot-Lackmann, F. *J. Phys. Chem. Solids* **1968**, *29*, 1235−1243.

(59) Burdett, J. K.; Lee, S. *J. Am. Chem. Soc.* **1985**, *107*, 3050−3063.

(60) Pettifor, D. G. *Bonding and Structure of Molecules and Solids*, 1st ed.; Oxford University Press: New York, 1995.

(61) Cyrot-Lackmann, F. *J. Phys., Colloq.* **1974**, *35*, 109−114.

(62) Michael Clark, P.; Lee, S.; Fredrickson, D. C. *J. Solid State Chem.* **2005**, *178*, 1269−1283.

(63) Phillips, R.; Carlsson, A. E. *Phys. Rev. B* **1990**, *42*, 3345.

(64) Seiser, B.; Hammerschmidt, T.; Kolmogorov, A. N.; Drautz, R.; Pettifor, D. G. *Phys. Rev. B* **2011**, *83*, 224116.

(65) Nilsson, A.; Pettersson, L. G. M.; Norskov, J. *Chemical Bonding at Surfaces and Interfaces*; Elsevier Science: Amsterdam, 2007.

(66) Okamoto, H. *J. Phase Equilib.* **2002**, *23*, 549−550.

(67) What would happen if there were even thicker layers? Some Ti and Cu sites would lose all heteroatomic contacts, thus causing these atoms to gain little neutralization in phase formation. The two atom layer thickness presents a balance of homoatomic and heteroatomic bonding to deliver a neutralizing effect.

(68) Murray, J. L. In *Binary Alloy Phase Diagrams*; Massalski, T. B., Ed.; ASM International: Materials Park, OH, 1990; Vol. 3, pp 2615−2617.

(69) The retention of the Ti atoms' neutralization within $TiMn_2$ is also linked to bond lengths. Within the CsCl structure, Ti is coordinated by 8 Mn atoms at a distance of 2.57 Å. Within the $TiMn_2$ structure, Ti gains 4 more Mn contacts to form a truncated tetrahedron around each Ti atom, but these distances are 2.77 Å on average. This tradeoff between number of neighbors and distances allows the Ti atoms to preserve their $\mu_2^{\text{A-B}}/\mu_2$ ratio and maintain their low RAs.

(70) Following the removal of one Mn atom, the average Mn−Mn distance for these sites shortens relative to those in the $TiMn_2$ bulk phase (2.37 Å compared to 2.43 Å). Reducing these distances dampens the effect of losing a Mn neighbor on the $\mu_2^{\text{Mn-Mn}}$ so that the Mn sites get only the slight bump in the $\mu_2^{\text{Mn-Ti}}/\mu_2$ necessary for almost perfect neutrality.

(71) To estimate this increase, we can solve for how much a single Ti atom will increase the $\mu_2^{\text{A-A}}$ for a given Ti site within $Ti_{21}Mn_{25}$. The Ti site within the $TiMn_2$ fragment has only 4 close contacts of equal distance. Dividing its $\mu_2^{\text{Ti-Ti}}$ value by 4 approximates the electronic effect of one close Ti contact. This amount is then multiplied by the number of extra contacts gained from adopting tetrahedral packing and added to the $\mu_2^{\text{Ti-Ti}}$ of the helix sites.

(72) Miessler, G. L.; Tarr, D. A. *Inorganic Chemistry*; 4th ed.; Prentice Hall: Upper Saddle River, NJ, 2010.

(73) Lowry, T. M. *J. Soc. Chem. Ind., London* **1923**, *42*, 43−47.

(74) Brønsted, J. *Recl. Trav. Chim. Pays-Bas* **1923**, *42*, 718−728.

(75) Lewis, G. N. *Valence and the Structure of Atoms and Molecules*; The Chemical Catalog Company: New York, 1923.

(76) Jensen, W. B. *The Lewis Acid-Base Concepts: An Overview*; Wiley: New York, 1980.

(77) Pearson, R. G. *Chemical Hardness: Applications from Molecules to Solids*, 1st ed.; Wiley-VCH: New York, 1997.

(78) Samson, S. *Nature* **1962**, *195*, 259−262.

(79) Samson, S. *Acta Crystallogr.* **1965**, *19*, 401−413.

(80) Samson, S. *Acta Crystallogr.* **1967**, *23*, 586−600.

(81) Weber, T.; Dshemuchadse, J.; Kobas, M.; Conrad, M.; Harbrecht, B.; Steurer, W. *Acta Crystallogr., Sect. B* **2009**, *65*, 308−317.

(82) Conrad, M.; Harbrecht, B.; Weber, T.; Jung, D. Y.; Steurer, W. *Acta Crystallogr., Sect. B* **2009**, *65*, 318−325.

(83) Fredrickson, D. C.; Lee, S.; Hoffmann, R. *Angew. Chem., Int. Ed.* **2007**, *46*, 1958−1976.

(84) Forsyth, J. B.; D' Alte da Veiga, L. M. *Acta Crystallogr.* **1962**, *15*, 543−546.

(85) Fredrickson, D. C. *J. Am. Chem. Soc.* **2012**, *134*, 5991−5999.

(86) Mott, N. F.; Jones, H. *The Theory of the Properties of Metals and Alloys*; Dover Publications: New York, 1958.